Journal of Low Temperature Physics (2024) 214:344–359
https://doi.org/10.1007/s10909-024-03047-8

Seebeck Power Generation and Peltier Cooling in a Normal Metal-Quantum Dot-Superconductor Nanodevice

Sachin Verma[1] · **Ajay Singh**[1]

Received: 16 September 2023 / Accepted: 1 January 2024 / Published online: 7 February 2024

Abstract
We theoretically investigate the Seebeck and Peltier effect across an interacting quantum dot (QD) coupled between a normal metal and a Bardeen–Cooper–Schrieffer superconductor within the Coulomb blockade regime. Our results demonstrate that the thermoelectric conversion efficiency at optimal power output (optimized with respect to QD energy level and external serial load) in NQDS nanodevice can reach up to $58\%\eta_C$, where η_C is Carnot efficiency, with output power $P_{max} \approx 35$ fW for temperature below the superconducting transition temperature. Further, the Peltier cooling effect is observed for a wide range of parameter regimes, which can be optimized by varying the background thermal energy, QD level energy, QD-reservoir tunneling strength, and bias voltage. The results presented in this study are within the scope of existing experimental capabilities for designing miniature hybrid devices that operate at cryogenic temperatures.

Keywords Quantum dot · Superconductivity · Andreev bound states · Coulomb blockade · Seebeck effect · Peltier effect

1 Introduction

In recent years, thermoelectric effects and heat transport in superconductor-quantum dot (QD)-based hybrid nanodevices has received significant attention due to its potential applications in energy harvesting and cooling at the nanoscale [1–22]. These hybrid devices combine quantum dots, superconductors, normal metals, or ferromagnetic materials and have emerged as promising platforms for studying

✉ Sachin Verma
sverma2@ph.iitr.ac.in

✉ Ajay Singh
ajay@ph.iitr.ac.in

[1] Department of Physics, India Institute of Technology Roorkee, Roorkee, Uttarakhand 247667, India

charge and heat transport at the nanoscale. The addition of superconducting components introduces novel features, such as diverging quasiparticle density of states near the edge of the superconducting energy gap, the formation of subgap Andreev bound states, and proximity-induced superconductivity, which can significantly impact the transport properties of the system [18, 23]. The operation of hybrid QD-based mesoscopic devices is based on phenomena that appear only at cryogenic temperatures [24–26]. Thus, these devices must be cooled down to a few Kelvin or lower temperatures. However, it also has the advantage that these low-dimensional devices are often more efficient than their bulk counterparts [27–30]. Further, the gate-tunable discrete energy levels of QD serve as perfect energy filters for electron transport, resulting in improved thermoelectric performance [31–36].

In superconductor-QD nanodevices, the Seebeck effect, which describes the generation of a voltage difference across a temperature gradient, i.e., system works as a particle exchange heat engine or power generator (see Fig. 1a), has been studied in a few papers [1, 6, 13, 18, 19]. Recently, it has been shown that a hybrid superconductor-QD nanodevice exhibits the Peltier effect, which refers to the creation or absorption of heat at the QD-reservoirs junction (see Fig. 1b), and the system works as a cooler [22]. Few studies have also explored the charge and spin Seebeck diode effect [5], cross thermoelectric effect [3], heat transport [14, 17, 18], and thermophase Seebeck effect [9, 21] in hybrid superconductor-QD nanodevices. Moreover, thermoelectric effects and heat transport in multi-terminal and multi-dot configurations in the presence of superconducting component have also been explored by several authors [2, 8, 10, 15, 16, 20].

In the present work, we examine nonlinear Seebeck power generation and Peltier cooling effect in N-QD-S nanodevice using the equation of motion technique within the Hubbard-I approximation and Keldysh non-equilibrium Green's function (NEGF) formalism [18, 37–39]. The term 'nonlinear regime' refers specifically to the situation when applied bias voltage and/or temperature gradient is finite, and Onsager linear response relations, provided in references [3, 13, 18], are not valid. While previous studies have explored similar setups, the optimal performance of the superconductor-QD-based thermoelectric particle exchange heat engine has not been studied so far. Therefore, in the present work, we contribute to previous studies by analyzing the nonlinear transport regime and the effect of the external load resistance on the practical optimization of the performance of the N-QD-S heat engine. Further, through a comprehensive analysis, the present study sheds light on the relatively unexplored regime of heat current or the Peltier cooling effect in N-QD-S nanodevice. This includes the impact of various system parameters on the Joule heating and Peltier cooling effect in the presence of on-dot Coulomb interaction.

This paper is structured as follows: Section 2 discusses the effective model Hamiltonian and theoretical formalism. Section 3 contains the numerical results and explanation for heat and thermoelectric transport. Section 4 concludes the present work.

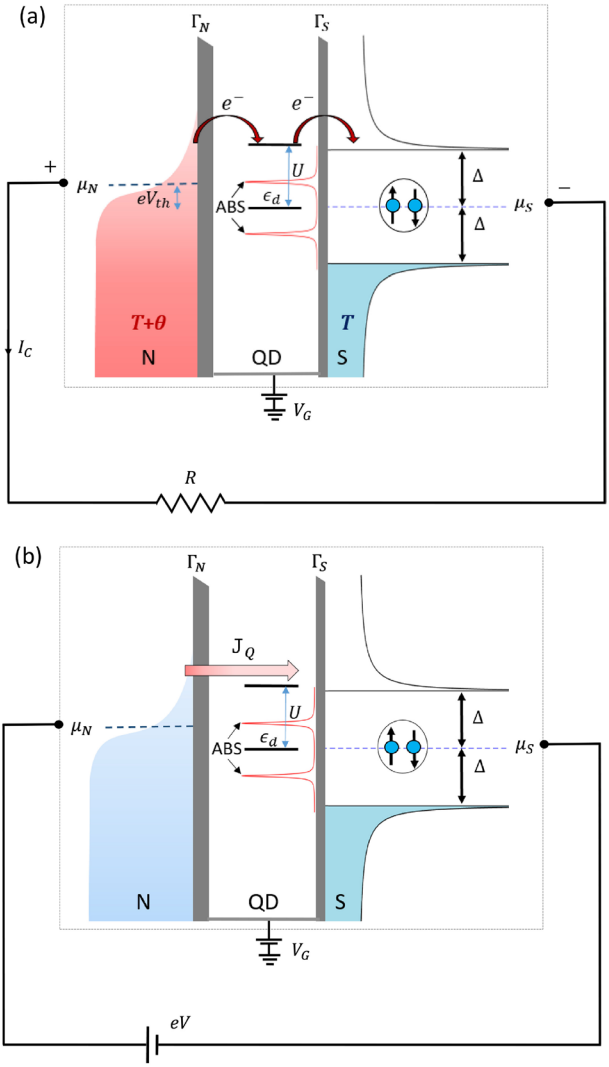

Fig. 1 **a** Energy diagram illustrating the hybrid N-QD-S particle exchange heat engine. The superconducting reservoir (S) has a finite energy gap Δ; single electrons or quasiparticles fill the states below the energy gap. At the QD-superconductor interface, electron and hole retro-reflections build up Andreev bound state (ABS), leading to a finite subgap charge and heat current. The gate-tunable discrete QD energy level ϵ_d (with on-site Coulomb repulsion U) serves as an ideal energy filter for electron transport. Due to a finite temperature difference θ, electrons tunnel from the normal reservoir (N) to the QD energy level (with tunneling rate Γ_N) and then to the superconducting reservoir (with tunneling rate Γ_S), producing a thermovoltage $V_{\rm th}$. Due to this thermovoltage, the power generated by the heat engine ($P = -I_C V_{\rm th} = I_C^2 R$) is available for consumption in external serial load R. **b** Energy diagram illustrating the N-QD-S cooler wherein a QD-superconductor hybrid structure with an applied bias voltage $\mu_N - \mu_S = eV$ and the gate-tunable QD energy level ϵ_d is used to cool ($J_Q > 0$) the normal metallic reservoir (N)

2 Model Hamiltonian and Theoretical Description

The N-QD-S system is modeled by single impurity Anderson model and Bogoliubov transformed BCS mean-field Hamiltonian [18],

$$\begin{aligned} H = &\sum_{k,\sigma} \epsilon_{k,N} c^{\dagger}_{k\sigma,N} c_{k\sigma,N} + \sum_{k,\sigma} E_k \gamma^{\dagger}_{k\sigma} \gamma_{k\sigma} + \sum_{\sigma} \epsilon_d n_\sigma + U n_\uparrow n_\downarrow + \\ &\sum_{k\sigma} (\mathcal{V}_{k,N} d^{\dagger}_{\sigma} c_{k\sigma,N} + \mathcal{V}^{*}_{k,N} c^{\dagger}_{k\sigma,N} d_\sigma) + \sum_{k\sigma} (\mathcal{V}_{k,S} u^{*}_{k} d^{\dagger}_{\sigma} \gamma_{k\sigma} + \mathcal{V}^{*}_{k,S} u_k \gamma^{\dagger}_{k\sigma} d_\sigma) + \\ &\sum_{k} [\mathcal{V}^{*}_{k,S} v_k (d^{\dagger}_{\uparrow} \gamma^{\dagger}_{-k\downarrow} - d^{\dagger}_{\downarrow} \gamma^{\dagger}_{k\uparrow}) + \mathcal{V}_{k,S} v^{*}_{k} (\gamma_{-k\downarrow} d_\uparrow - \gamma_{k\uparrow} d_\downarrow)] \end{aligned} \tag{1}$$

The first term describes the normal metallic reservoir in the non-interacting quasiparticle approximation with single-electron kinetic energy $\epsilon_{k,N}$ and $c_{k\sigma,N}(c^{\dagger}_{k\sigma,N})$ is the annihilation(creation) operator of an electron with spin σ and wave vector $\mathbf{k}$.

The second term describes the superconducting reservoir, where $\gamma_{k\sigma}(\gamma^{\dagger}_{k\sigma})$ is the annihilation(creation) operator for Bogoliubov quasiparticles with spin σ, wave vector $\mathbf{k}$ and energy $E_k = \sqrt{\epsilon^2_{k,S} + |\Delta|^2}$. The temperature dependence of the superconducting energy gap is given as $\Delta(T) = \Delta_0 \, tanh\left(1.74\sqrt{(T_c/T) - 1}\right)$, where Δ_0 is superconducting energy gap at absolute zero temperature and T_c is critical temperature with $k_B T_c = 0.568\Delta_0$ [17].

Third term describes the Hamiltonian for single-level QD with energy ϵ_d, and $d_\sigma(d^{\dagger}_{\sigma})$ is the annihilation(creation) operator of electron with spin σ on the QD and $n_\sigma = d^{\dagger}_{\sigma} d_\sigma$ is number operator. The QD can have maximum occupancy of two electrons with opposite spins. We also consider the intradot electron–electron Coulomb repulsion with the interaction strength U represented by the fourth term.

The remaining terms represents the tunneling Hamiltonian between the QD energy level and reservoirs with $\mathcal{V}_{k\alpha}$ as the tunneling amplitude between the QD and the α-reservoir ($\alpha \in N, S$). The coefficients u_k and v_k read

$$|u_k|^2 = \frac{1}{2}\left(1 + \frac{\epsilon_{k,S}}{\sqrt{\epsilon^2_{k,S} + |\Delta|^2}}\right) \quad \& \quad |v_k|^2 = \frac{1}{2}\left(1 - \frac{\epsilon_{k,S}}{\sqrt{\epsilon^2_{k,S} + |\Delta|^2}}\right) \tag{2}$$

In order to study the thermoelectric transport properties of N-QD-S system using model Hamiltonian in Eqn. (1), we apply the Keldysh non-equilibrium Green's function formalism [38] (see appendix). To truncate hierarchy of Green's function equation of motions, we use Hubbard-I approximation [18, 37], which is good enough to describe the Coulomb blockade regime at temperatures $T >> T_K$, where T_K is Kondo temperature. Furthermore, we assume that the coupling strength $\mathcal{V}_{k,\alpha}$ is momentum independent. Therefore, the tunneling rate from the dot to the α-leads is represented as $\Gamma_\alpha = 2\pi|\mathcal{V}_\alpha|^2\rho_{0\alpha}$, where the density of states in normal metallic state $\rho_{0\alpha}$ remains constant within a range of energy around the Fermi level (wide-band limit).

After self-consistent calculation of the occupancy and Green's function of the QD (as described in the appendix), the nonlinear thermoelectric transport properties can be calculated as follows. It has been shown in previous works that the Onsager linear approximation quickly fails, implying that the thermovoltage, thermopower, and output power in the N-QD-S system are inherently nonlinear [3, 18]. Therefore, in the present work, the nonlinear thermoelectric transport properties have been calculated using the general charge and heat current formulas [38, 40–43]. Let the system is under the influence of finite voltage $V = (\mu_N - \mu_S)/e$ (say $\mu_N = eV$ and $\mu_S = 0$) and/or temperature gradient $T_N - T_S = \theta$ (say $T_N = T + \theta$ and $T_S = T$). Then, the charge current I_C and heat current J_Q from left to right reservoir across the QD can be expressed as

$$I_C = I_A + I_{QP}; \tag{3}$$

with

$$I_A = \frac{2e}{h}\int \big[f_N(\omega - eV, T+\theta) - f_N(\omega + eV, T+\theta)\big] T_A(\omega)\, d\omega$$
$$I_{QP} = \frac{2e}{h}\int \big[f_N(\omega - eV, T+\theta) - f_S(\omega, T)\big] T_{QP}(\omega)\, d\omega$$

and

$$J_Q = J_A + J_{QP}; \tag{4}$$

with

$$J_A = \frac{-4\ eV}{h}\int \big[f_N(\omega - eV, T+\theta) - f_N(\omega + eV, T+\theta)\big] T_A(\omega)\, d\omega = -2VI_A$$
$$J_{QP} = \frac{2}{h}\int (\omega - eV)\big[f_N(\omega - eV, T+\theta) - f_S(\omega, T)\big] T_{QP}(\omega)\, d\omega$$

Where $I_A(I_{QP})$ and $J_A(J_{QP})$ are Andreev (quasiparticle) contribution to charge and heat current, respectively.

$T_A(\omega) = \Gamma_N^2 |G^r_{d,12}(\omega)|^2$ is the Andreev tunneling amplitude and $T_{QP}(\omega) = \frac{\Gamma_N\Gamma_S|\omega|}{\sqrt{\omega^2-\Delta^2}}\,\theta(|\omega|-\Delta) \times \left[|G^r_{d,11}(\omega)|^2 + |G^r_{d,21}(\omega)|^2 - \frac{2\Delta}{|\omega|} Re(G^r_{d,11}(\omega)\, G^a_{d,12}(\omega))\right]$ is the quasiparticle tunneling amplitude.

In order to use N-QD-S as a heat engine or power generator, the temperature gradient θ is set larger then zero. Due to this temperature difference electrons move from left reservoir to the right reservoir and thus create a potential difference ($\mu_N - \mu_S = eV_{\text{th}}$) due to accumulation of electrons on the right reservoir and positive charge to the left reservoir. The thermovoltage (V_{th}) is determined from the condition [31, 32]

$$I_C(V_{\text{th}}, \theta) + \frac{V_{\text{th}}}{R} = 0 \tag{5}$$

in the presence of external serial load resistance R. Equation (5) is solved numerically to obtain $V_{\rm th}$ and eventually thermopower $S = \frac{V_{\rm th}}{\theta}$ and thermal conductance $K = \frac{J_Q}{\theta}$. The finite power output $P = -I_C V_{\rm th} = I_C^2 R$ generated by the heat engine dissipates across R. The thermoelectric efficiency is defined as the ratio between the generated output power and the nonlinear input heat current, i.e., $\eta = P/J_Q$.

The maximum power output $P_{\rm max}$ is calculated by optimizing $V_{\rm th}$ and ϵ_d for different values of external load R and the relative efficiency at maximal power output is given by,

$$\left(\frac{\eta_{P_{\rm max}}}{\eta_{\rm C}}\right) = \frac{P_{\rm max}}{J_Q} \times \frac{T+\theta}{\theta} \tag{6}$$

where $\eta_{\rm C} = \frac{\theta}{T+\theta}$ is upper bound Carnot efficiency of the heat engine.

Based on the Peltier effect, the total heat flow $J_Q = J_{QP} + J_A$ removes or adds heat to the normal metal, causing the temperature of the normal metal to decrease or increase, and the system can work as a cooler or refrigerator.

In the linear response regime, i.e., for infinitesimally small bias voltage between the reservoirs, the Fermi function of the normal and the superconducting reservoirs can be expanded around the equilibrium value (average T with Fermi level $\mu_f = 0$), which gives the charge and heat current satisfying the Onsager relations [3, 13, 18]. Note that the heat current J_Q in Onsager linear response relation is independent of the Andreev tunneling $T_A(\omega)$; therefore, Andreev tunneling does not contribute to heat current in the linear response regime. Further, beyond the linear response regime, the Andreev heat current J_A does not contain the energy current, unlike the quasiparticle current J_{QP}. This is due to the intrinsic particle-hole symmetry present in the subgap regime. In fact, the Andreev tunneling $T_A(\omega)$ is always particle-hole symmetric, i.e., $T_A(\omega) = T_A(-\omega)$, even if the finite gate voltage is applied to the quantum dot. This is in contrast to the quasiparticle tunneling where $T_{QP}(\omega) \neq T_{QP}(-\omega)$ for finite gate voltages away from the particle-hole symmetry point. Therefore, the Andreev bound states only contribute to the Joule heating or heat dissipation, and the cooling effect is entirely due to quasiparticle tunneling.

3 Result and Discussion

Numerical calculations for the nonlinear thermoelectric quantities are done using MATLAB based on the equations derived in the previous section and $\Gamma_0(1\,meV)$ is considered as the energy unit. We analyze two situations: (1) In Fig. 2, we discuss the optimal power output and corresponding thermoelectric efficiency of the N-QD-S particle exchange heat engine, and (2) In Figs. 3 and 4, we consider a voltage-driven case for isothermal reservoirs and discuss the total heat current and Peltier cooling power as a function of various system parameters.

Figure 2 shows the variation of maximum power output $P_{\rm max}$ (maximize with respect to the QD energy level ϵ_d or gate voltage) and normalized efficiency

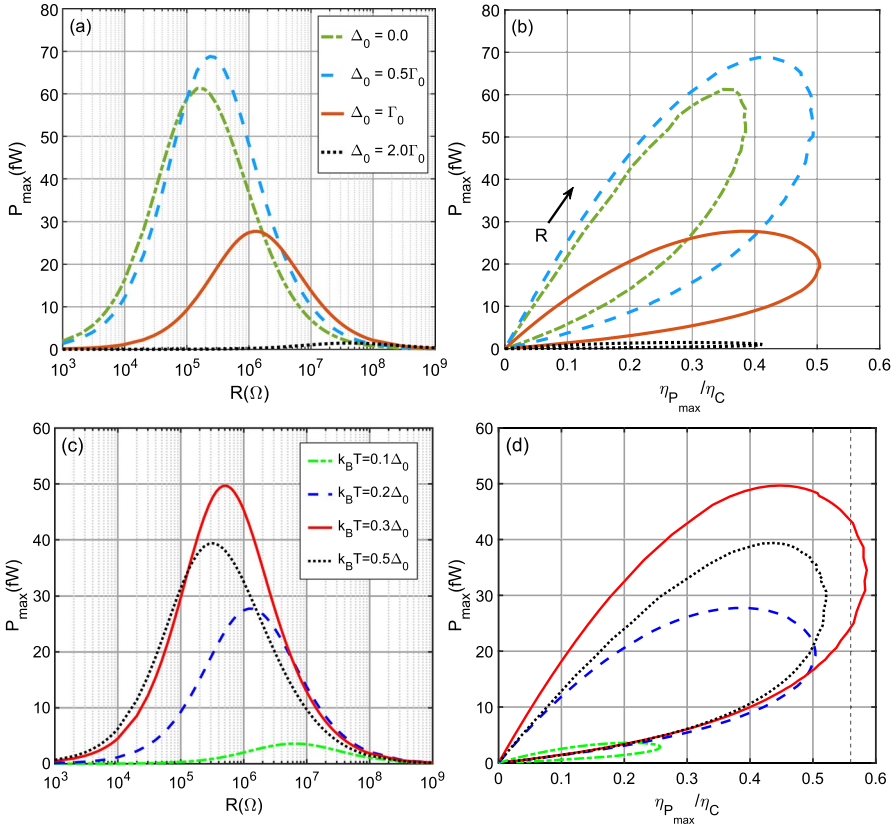

Fig. 2 **a** $P_{\max}$ as a function of external load R, and (b) $P_{\max}$ as a function of $\eta_{P_{\max}}$ for different Δ_0. The other parameters in (**a**) and (**b**) are: $U = 2.0\Gamma_0$, $\Gamma_S = \Gamma_N = 0.1\Gamma_0$, $k_BT = 0.2\Gamma_0$, and $k_B\theta = 0.1\Gamma_0$. **c** $P_{\max}$ as a function of R, and (b) $P_{\max}$ as a function of $\eta_{P_{\max}}$ for different k_BT. The vertical black dashed lines at $\eta_{P_{\max}} = 0.54\eta_C$ indicate the Curzon-Ahlborn efficiency, i.e., $\eta_{CA} = 1 - \sqrt{T/(T+\theta)}$. The other parameters in (**c**) and (**d**) are: $\Delta_0 = \Gamma_0$, $U = 2.0\Gamma_0$, $\Gamma_S = \Gamma_N = 0.1\Gamma_0$ and $k_B\theta = 0.1\Gamma_0$. The arrow indicates the direction for increasing external load R

corresponding to the maximum power $\eta_{P_{\max}}$ of the N-QD-S particle exchange heat engine beyond the linear response regime for different values of superconducting energy gap Δ_0, background thermal energy k_BT and external serial load R. It is important to highlight here that Andreev tunneling does not contribute to the creation of thermovoltage (V_{th}) and only suppresses it within the superconducting energy gap. Further, the proximity-induced superconducting gap does not affect the thermoelectric transport properties for the parameter regimes considered in the present work. Therefore, $P_{\max}$ and $\eta_{P_{\max}}$ shown here are generated completely by the quasiparticle tunneling close to the edge of the superconducting energy gap [3, 13, 18].

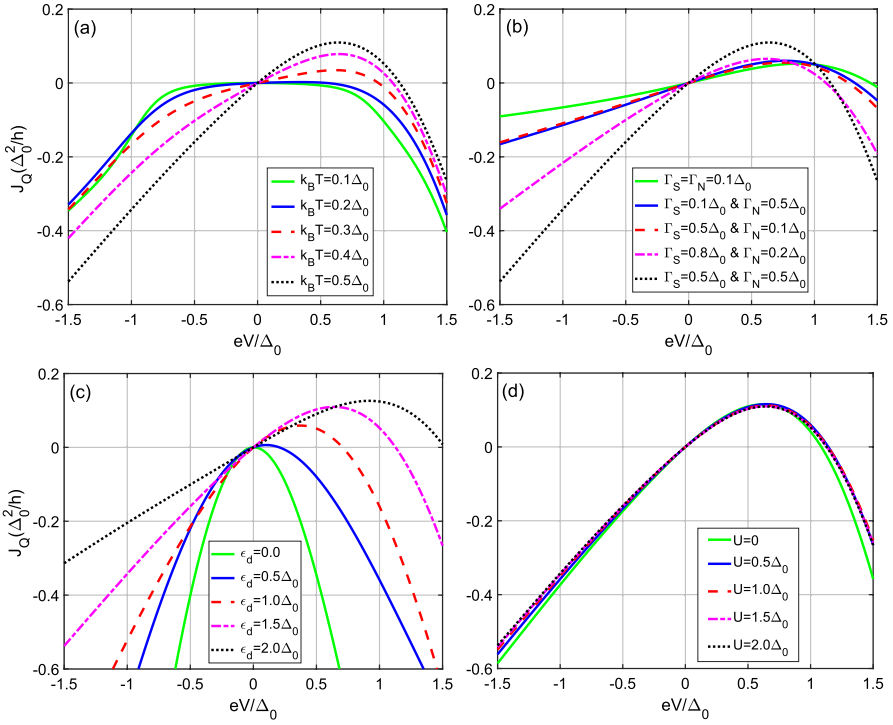

Fig. 3 Total heat current J_Q as a function of bias voltage eV for different (**a**) background thermal energies k_BT with $\Gamma_S = \Gamma_N = 0.5\Delta_0$, $\epsilon_d = 1.5\Delta_0$, $U = 2\Delta_0$, **b** QD-reservoirs tunneling rates Γ_S/Γ_N with $k_BT = 0.5\Delta_0$, $\epsilon_d = 1.5\Delta_0$, $U = 2\Delta_0$, **c** QD energy level ϵ_d with $k_BT = 0.5\Delta_0$, $\Gamma_S = \Gamma_N = 0.5\Delta_0$, $U = 2\Delta_0$, and **d** on-dot Coulomb interaction U with $k_BT = 0.5\Delta_0$, $\Gamma_S = \Gamma_N = 0.5\Delta_0$, $\epsilon_d = 1.5\Delta_0$

According to Fig. 2a, for a relatively small superconducting gap (say, $\Delta_0 = 0.5\Gamma_0$), the optimal power output ($P_{\max} \approx 70\,\text{fW}$) due to quasiparticle tunneling is larger than the optimal value of $P_{\max}$ for NQDN system ($\Delta_0 = 0$). Such enhancement in power output is attributed to the diverging quasiparticle density of states near the edge of the superconducting energy gap. However, as Δ_0 increases, a large thermal energy or thermal gradient is required for quasiparticle tunneling, and hence the thermovoltage (V_{th}) and $P_{\max}$ are significantly reduced. For $\Delta_0 = 2\Gamma_0$, the optimal $P_{\max}$ becomes of the order of few fW. Further, as Δ_0 increases, the optimal load, i.e., R corresponding to the peak in $P_{\max}$, shifts toward larger values due to the load matching. The optimal load shifts from approximately $100k\Omega$ to $100M\Omega$ as Δ_0 increases from 0 to $2\Gamma_0$. Similar to the maximum power output $P_{\max}$, for a relatively small superconducting gap, the corresponding thermoelectric efficiency $\eta_{P_{\max}}$ for the N-QD-S system is greater as compared to the NQDN system, with optimal $\eta_{P_{\max}} \approx 50\%\eta_C$ as shown in Fig. 2b. As Δ_0 is increased from $0.5\Gamma_0$ to Γ_0, the value of optimal $\eta_{P_{\max}}$ remains almost constant and for $\Delta_0 = \Gamma_0$, optimal $\eta_{P_{\max}}$ reduces by approximately $20\%\eta_C$.

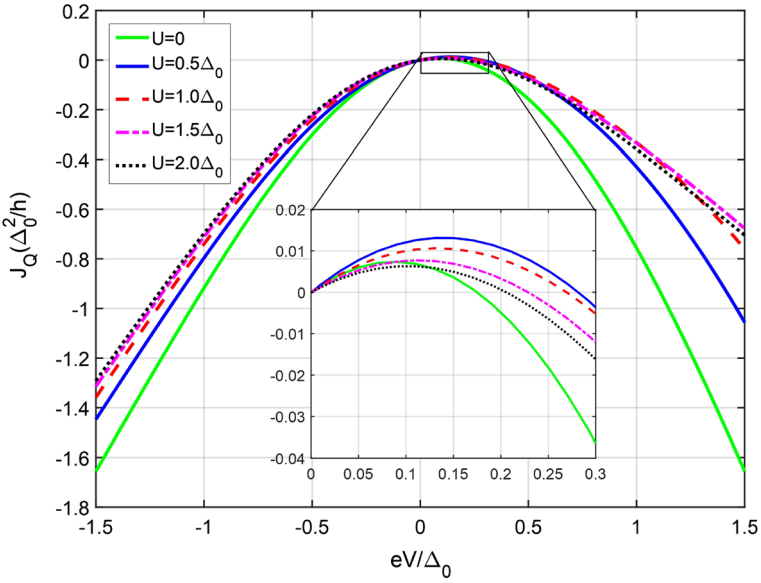

Fig. 4 Total heat current J_Q as a function of bias voltage eV for different on-dot Coulomb interaction U with $k_BT = 0.5\Delta_0$, $\Gamma_S = \Gamma_N = 0.5\Delta_0$, and $\epsilon_d = 0.5\Delta_0$. The inset shows the close-up view for the low bias voltage, i.e., $eV < 0.3\Delta_0$, where the Peltier cooling of the normal metallic reservoir is U dependent

As background thermal energy k_BT increases, initially, $P_{\max}$ is enhanced due to increasing quasiparticle tunneling from the normal metallic side, as seen in Fig. 2c. When k_BT approaches the energy corresponding to the superconducting transition temperature k_BT_c, the $P_{\max}$ begins to decrease due to backward hole tunneling from the superconducting side. The thermoelectric efficiency $\eta_{P_{\max}}$ in Fig. 2d follows a similar behavior as that of $P_{\max}$ with increasing k_BT. The normalized $\eta_{P_{\max}}$ can reach up to $58\%\eta_C$ with power output ≈ 35 fW for $k_BT = 0.3\Delta_0$ and $k_B\theta = 0.1\Delta_0$.

It is important to note that the optimal value of ϵ_d corresponds to the diverging quasiparticle density of states near the edge of the superconducting energy gap. The on-dot Coulomb interaction U primarily affects the subgap regime and Andreev tunneling, while U has a negligible effect on the power output and efficiency generated by quasiparticles tunneling close to the edge of the superconducting energy gap, i.e., $\epsilon_d \gtrsim \Delta_0$ [9, 13, 18].

Figure 3 shows the variation of nonlinear heat current $J_Q = J_A + J_{QP}$ given in Eqn. (4) as a function of bias voltage(both forward and reverse bias) for different values of background thermal energy k_BT, QD-reservoir tunneling strengths Γ_S/Γ_N, QD level energy ϵ_d and on-dot Coulomb interaction U. The Peltier cooling effect occurs when $J_Q > 0$, i.e., heat is absorbed from the normal metallic side. If $J_Q < 0$, then Joule heating is dominant, and hence, the applied voltage bias only heats the normal metallic reservoir. As discussion in Sect. 2, the Andreev bound states only contribute to the Joule heating or heat dissipation, and the cooling effect is entirely due to quasiparticle tunneling.

Figure 3a shows the heat current J_Q as a function of bias voltage eV for different values of the background thermal energy k_BT. At low background thermal energies, i.e., $k_BT \leq 0.1\Delta_0$, no cooling effect ($J_Q > 0$) is observed as the quasiparticle tunneling is strongly suppressed and Andreev Joule heating is significant. In this case, the heat current only consists of Joule heating ($J_Q < 0$) generated by Andreev and quasiparticle currents and has been analyzed in reference [18]. Now, for higher temperatures, i.e., $k_BT = 0.3\Delta_0$ and $k_BT = 0.5\Delta_0$ the cooling effect is observed for the forward bias (positive) voltage within the superconducting energy gap, i.e., $eV \lesssim \Delta_0$. The cooling effect is maximum as k_BT approaches the superconducting transition temperature due to vanishing Andreev current or Joule heating. Now, for large voltages ($eV \gtrsim \Delta_0$), the quasiparticle Joule heating predominates, and the cooling effect ceases. The negative bias voltage ($eV < 0$) only heats the normal metal reservoir without Peltier cooling.

In Fig. 3b, the heat current J_Q shows the cooling effect when total coupling strength $\Gamma_N + \Gamma_S$ is varied from $0.1\Delta_0$ to Δ_0. The cooling effect for $eV < \Delta_0$ and $\Gamma_N + \Gamma_S \leq 0.6\Delta_0$ is nearly independent of the ratio Γ_S/Γ_N and attains a relatively large magnitude for the strong symmetric coupling configuration with $\Gamma_N + \Gamma_S = \Delta_0$ as considered in reference [22].

Figure 3c shows the heat current J_Q as a function of bias voltage eV for different values of the QD level position ϵ_d. When ϵ_d lies within the superconducting gap, i.e., $\epsilon_d < \Delta_0$, the Andreev and quasiparticle current generates large Joule heating effects even at low bias voltages. The Peltier cooling effect caused by the quasiparticles begins to dominate and extends to the larger bias voltage as the position of QD energy level ϵ_d is tuned far above the Fermi energy level, i.e., $\epsilon_d \gtrsim \Delta_0$. However, as Fig. 3d illustrates, the heat current J_Q, which includes the Joule heating current and the cooling effect, is independent of the strength of the on-dot Coulomb interaction U when the QD energy level is outside the superconducting energy gap, i.e., $\epsilon_d = 1.5\Delta_0$. The independence of the heat current, and other thermoelectric quantities on the coulomb interaction strength U for $\epsilon_d \gtrsim \Delta_0$ is consistent with previous results [9, 13, 18].

Figure 4 shows the heat current J_Q as a function of bias voltage eV for different values of the on-dot Coulomb interaction U when the QD energy level lies within the superconducting gap, i.e., $\epsilon_d = 0.5\Delta_0$. For $\epsilon_d < \Delta_0$, the magnitude of Joule heating (largely due to Andreev tunneling) and Peltier cooling (due to quasiparticle tunneling) depends on the on-dot Coulomb interaction U. The U dependence of the heat current can be explained by considering effective QD energy levels. For interacting QD ($U > 0$), two effective levels lie at ϵ_d and $\epsilon_d + U$. For the non-interacting case ($U = 0$), the effective QD energy level $\epsilon_d = 0.5\Delta_0$ lies close to the Fermi level $\mu_f = 0$ within the superconducting energy gap. Therefore, the magnitude of the heat current is enhanced due to the substantial Andreev tunneling amplitude. This Andreev tunneling amplitude diminishes as the Coulomb interaction U increases, displacing the effective quantum dot energy levels away from $\mu_f = 0$ and subsequently reducing the heat current magnitude. When the on-dot Coulomb interaction is relatively strong ($U \geq \Delta_0$), one of the effective quantum dot energy levels lies beyond the superconducting energy gap, resulting in a heat current independent of U (as discussed in

Fig. 3d above). The Peltier cooling effect ($J_Q > 0$ for $eV < 0.3\Delta_0$), caused by the quasiparticles, dominates when one of the effective QD energy levels aligns with the diverging quasiparticle density of states near the edge of the superconducting gap, i.e., $\epsilon_d + U \approx \Delta_0$ ($U = 0.5\Delta_0$ in the present case). For non-interacting QD ($U = 0$), the effective energy levels are positioned entirely within the superconducting energy gap, i.e., $\epsilon_d = 0.5\Delta_0$. Consequently, the Peltier cooling of the normal metallic reservoir, resulting from quasiparticle tunneling at low bias, is reduced.

4 Conclusion

In summary, we have presented a theoretical study of the (1) Seebeck effect and (2) Peltier effect in a hybrid N-QD-S nanodevice based on an interacting quantum dot coupled between a normal metal and Bardeen–Cooper–Schrieffer superconductor.

In the first case, we show that the presence of a superconducting energy gap (Δ_0) significantly affects the maximum power output ($P_{\max}$) and corresponding thermoelectric efficiency ($\eta_{P_{\max}}$). For smaller superconducting energy gap ($\Delta_0 \leq 0.5\Gamma_0$), quasiparticle tunneling led to higher $P_{\max}$ values compared to the N-QD-N case ($\Delta_0 = 0$). However, as Δ_0 increases, significant thermal energy k_BT or thermal gradient $k_B\theta$ is required for quasiparticle tunneling. As a result, $P_{\max}$ and $\eta_{P_{\max}}$, which are due to quasiparticle tunneling near the edge of the superconducting energy gap, are significantly reduced. Background thermal energy (k_BT) also played a crucial role, enhancing $P_{\max}$ initially but decreasing it as k_BT approached the energy corresponding to superconducting transition temperature k_BT_c due to backward hole tunneling from the superconducting side.

In the second case, we analyzed nonlinear heat current (J_Q) as a function of bias voltage and other system parameters. The Peltier cooling ($J_Q > 0$) of the normal source reservoir is observed for positive bias voltage ($eV > 0$), with maximum cooling occurring as k_BT approaches k_BT_c. The coupling strength between the quantum dot and reservoirs influenced the heat current, with symmetric and strong coupling configurations leading to larger cooling magnitudes. Additionally, if the quantum dot energy level (ϵ_d) lies within the superconducting gap, Joule heating effects are significant. For, $\epsilon_d \gtrsim \Delta_0$, the Peltier cooling effect dominates and extends to higher bias voltages. The effect of on-dot Coulomb interaction on the heat current became negligible for $\epsilon_d \gtrsim \Delta_0$. However, for $\epsilon_d < \Delta_0$, the magnitude of the heat current depends on the on-dot Coulomb interaction U. In particular, for bias voltages in the range $eV < 0.3\Delta_0$, the quasiparticles cause a relatively small Peltier cooling of the normal metallic reservoir. The maximum Peltier cooling is observed when, depending on the value of ϵ_d and U, one of the effective energy levels of the quantum dot aligns with the diverging quasiparticle density of states near the edge of the superconducting gap. Here, it is important to highlight that calculating the optimal cooling power involves optimizing not only ϵ_d , but also the change in the temperature of the normal metallic reservoir. This temperature change can be calculated using a phenomenological equation based on the thermal model, as described in reference [22, 24, 44], and will be considered in future studies. These results provide significant insights into the nonlinear Seebeck and Peltier effect

in N-QD-S nanodevice, with potential applications for the miniature on-chip power generators and refrigerators in cryogenic nanoelectronics.

Appendix

In this section, we present the calculation for the Green's functions and occupancy of the QD. In Nambu representation, we define the single particle retarded Green's function of the QD as a 2×2 matrices [45]

$$\mathbf{G}_d^r(\omega) = \left\langle\left\langle \begin{pmatrix} d_\uparrow \\ d_\downarrow^\dagger \end{pmatrix} \begin{pmatrix} d_\uparrow^\dagger & d_\downarrow \end{pmatrix} \right\rangle\right\rangle = \begin{pmatrix} \langle\langle d_\uparrow | d_\uparrow^\dagger \rangle\rangle & \langle\langle d_\uparrow | d_\downarrow \rangle\rangle \\ \langle\langle d_\downarrow^\dagger | d_\uparrow^\dagger \rangle\rangle & \langle\langle d_\downarrow^\dagger | d_\downarrow \rangle\rangle \end{pmatrix} = \begin{pmatrix} G_{d,11}^r(\omega) & G_{d,12}^r(\omega) \\ G_{d,21}^r(\omega) & G_{d,22}^r(\omega) \end{pmatrix}$$

where the diagonal components of $\mathbf{G}_d^r(\omega)$ represents the single particle retarded Green's function of electron with spin $\sigma = \uparrow$ and hole with spin $\sigma = \downarrow$, respectively. The off-diagonal component represents the superconducting paring correlation on the QD. The Fourier transform of the single particle retarded Green's function for QD

$$G_{d,11}^r(\omega) = \langle\langle d_\uparrow | d_\uparrow^\dagger \rangle\rangle = -\frac{i}{2\pi} \lim_{\delta \to 0^+} \int \theta(t) \langle \{ d_\uparrow(t), d_\uparrow^\dagger(0) \} \rangle e^{i(\omega + i\delta)t} dt$$

where $\theta(t)$ is Heaviside function, must satisfy the following EOM [38]

$$\omega \langle\langle d_\uparrow | d_\uparrow^\dagger \rangle\rangle = \langle \{ d_\sigma, d_\uparrow^\dagger \} \rangle + \langle\langle [d_\uparrow, H] | d_\uparrow^\dagger \rangle\rangle.$$

By evaluating different commutator and anti-commutator brackets we drive the following coupled equations for the single particle Green's functions

$$\left\{ \omega - \epsilon_d - \sum_k \frac{|\mathcal{V}_{k,N}|^2}{\omega - \epsilon_{k,N}} - \sum_k |\mathcal{V}_{k,S}|^2 \left(\frac{|u_k|^2}{\omega - E_k} + \frac{|v_k|^2}{\omega + E_k} \right) \right\} \langle\langle d_\uparrow | d_\uparrow^\dagger \rangle\rangle =$$
$$1 + \left\{ \sum_k |\mathcal{V}_{k,S}|^2 u_k^* v_k \left(\frac{1}{\omega - E_k} - \frac{1}{\omega + E_k} \right) \right\} \langle\langle d_\downarrow^\dagger | d_\uparrow^\dagger \rangle\rangle + U \langle\langle d_\uparrow n_\downarrow | d_\uparrow^\dagger \rangle\rangle$$

$$\left\{ \omega + \epsilon_d - \sum_k \frac{|\mathcal{V}_{k,N}|^2}{\omega + \epsilon_{k,N}} - \sum_k |\mathcal{V}_{k,S}|^2 \left(\frac{|u_k|^2}{\omega + E_k} + \frac{|v_k|^2}{\omega - E_k} \right) \right\} \langle\langle d_\downarrow^\dagger | d_\uparrow^\dagger \rangle\rangle =$$
$$\left\{ \sum_k |\mathcal{V}_{k,S}|^2 u_k v_k^* \left(\frac{1}{\omega - E_k} - \frac{1}{\omega + E_k} \right) \right\} \langle\langle d_\uparrow | d_\uparrow^\dagger \rangle\rangle - U \langle\langle d_\downarrow^\dagger n_\uparrow | d_\uparrow^\dagger \rangle\rangle$$

$$\left\{\frac{\omega-\epsilon_d-U}{\langle n_\downarrow\rangle}\right\}\langle\langle d_\uparrow n_\downarrow|d_\uparrow^\dagger\rangle\rangle = 1+\left\{\sum_k|\mathcal{V}_{k,S}|^2u_k^*v_k\left(\frac{1}{\omega-E_k}-\frac{1}{\omega+E_k}\right)\right\}\langle\langle d_\downarrow^\dagger|d_\uparrow^\dagger\rangle\rangle$$
$$+\left\{\sum_k\frac{|\mathcal{V}_{k,N}|^2}{\omega-\epsilon_{k,N}}+\sum_k|\mathcal{V}_{k,S}|^2\left(\frac{|u_k|^2}{\omega-E_k}+\frac{|v_k|^2}{\omega+E_k}\right)\right\}\langle\langle d_\uparrow|d_\uparrow^\dagger\rangle\rangle$$

$$\left\{\frac{\omega+\epsilon_d+U}{\langle n_\uparrow\rangle}\right\}\langle\langle d_\downarrow^\dagger n_\uparrow|d_\uparrow^\dagger\rangle\rangle = \left\{\sum_k|\mathcal{V}_{k,S}|^2u_kv_k^*\left(\frac{1}{\omega-E_k}-\frac{1}{\omega+E_k}\right)\right\}\langle\langle d_\uparrow|d_\uparrow^\dagger\rangle\rangle$$
$$+\left\{\sum_k\frac{|\mathcal{V}_{k,N}|^2}{\omega+\epsilon_{k,N}}+\sum_k|\mathcal{V}_{k,S}|^2\left(\frac{|u_k|^2}{\omega-E_k}+\frac{|v_k|^2}{\omega+E_k}\right)\right\}\langle\langle d_\downarrow^\dagger|d_\uparrow^\dagger\rangle\rangle$$

The terms with summations over k appearing in above equations can be simplified by replacing $\sum_k \to \int \rho(\epsilon)d\epsilon$ and then solving these expressions using the complex contour integration in the wide-band limit. Finally after solving above coupled equations, we arrive at the expression for the retarded Green's function of electron with spin $\sigma =\uparrow$ and off-diagonal superconducting pairing correlation on the QD, i.e.,

$$G^r_{d,11}(\omega) = \frac{\alpha_1(\omega)}{\omega-\epsilon_d+\left(\frac{i\Gamma_N}{2}+\beta(\omega)\right)\alpha_1(\omega)-\frac{\alpha_1(\omega)\,\alpha_2(\omega)\left(\frac{\Delta}{|\omega|}\beta(\omega)\right)^2}{\omega+\epsilon_d+\left(\frac{i\Gamma_N}{2}+\beta(\omega)\right)\alpha_2(\omega)}}$$

$$G^r_{d,21}(\omega) = \frac{\alpha_2(\omega)\left(\frac{\Delta}{|\omega|}\beta(\omega)\right)}{\omega+\epsilon_d+\left(\frac{i\Gamma_N}{2}+\beta(\omega)\right)\alpha_2(\omega)}\times G^r_{d,11}(\omega)$$

where

$$\alpha_1(\omega) = 1+\frac{U\langle n_\downarrow\rangle}{\omega-\epsilon_d-U},\quad \alpha_2(\omega) = 1+\frac{U\langle n_\uparrow\rangle}{\omega+\epsilon_d+U}$$

and

$$\beta(\omega) = \frac{\Gamma_S}{2}\rho_S(\omega) = \frac{\Gamma_S}{2}\frac{\omega}{\sqrt{\Delta^2-\omega^2}}\theta(\Delta-|\omega|)+\frac{i\Gamma_S}{2}\frac{|\omega|}{\sqrt{\omega^2-\Delta^2}}\theta(|\omega|-\Delta)$$

where $\rho_S(\omega)$ is the modified BCS density of states, with the real part accounting for the Andreev bound states within the superconducting gap. The other matrix elements is given by $G^r_{d,22}(\omega) = -G^r_{d,11}(-\omega)^*$ and $G^r_{d,12}(\omega) = G^r_{d,21}(-\omega)^*$. These retarded Green's functions allow us to calculate the advanced and lesser/greater Green's functions and eventually the thermoelectric transport properties.

The average occupancy on the quantum dot ($\langle n_\uparrow\rangle$=$\langle n_\downarrow\rangle$ for non-magnetic system) is calculated using the self-consistent integral equation of the form

$$\langle n_\sigma \rangle = \frac{-i}{2\pi} \int_{-\infty}^{\infty} G^<_{d,11}(\omega) d\omega$$

where the lesser Green's function $G^<_d$ obeys the Keldysh equation [38, 39]

$$\mathbf{G}^<_{d\sigma}(\omega) = \mathbf{G}^r_{d\sigma}(\omega)\mathbf{\Sigma}^<(\omega)\mathbf{G}^a_{d\sigma}(\omega).$$

The advanced Green's function matrix is $\mathbf{G}^a_{d\sigma}(\omega) = \left[\mathbf{G}^r_{d\sigma}(\omega)\right]^\dagger$ and the lesser self-energy matrix is obtained using Ng ansatz [38, 46], i.e.,

$$\mathbf{\Sigma}^<(\omega) = -\sum_{\alpha \in N,S} \left[\mathbf{\Sigma}^r_\alpha - \mathbf{\Sigma}^a_\alpha\right] f_\alpha(\omega - \mu_\alpha)$$

This ansatz satisfies the continuity equation in steady state, allowing us to derive the lesser Green's function to examine the transport properties.

Now using retarded and advanced self-energy, we get

$$\mathbf{\Sigma}^<(\omega) = \begin{pmatrix} \Sigma^<_{11}(\omega) & \Sigma^<_{12}(\omega) \\ \Sigma^<_{21}(\omega) & \Sigma^<_{22}(\omega) \end{pmatrix}$$

with

$$\Sigma^<_{11}(\omega) = -i\Gamma_N f_N(\omega - \mu_N) - \frac{i\Gamma_S|\omega|}{\sqrt{\omega^2 - \Delta^2}} \theta(|\omega| - \Delta) f_S(\omega - \mu_S)$$

$$\Sigma^<_{12}(\omega) = \Sigma^<_{21}(\omega) = \frac{i\Gamma_S \Delta}{\sqrt{\omega^2 - \Delta^2}} \theta(|\omega| - \Delta) f_S(\omega - \mu_S)$$

$$\Sigma^<_{22}(\omega) = -i\Gamma_N f_N(\omega + \mu_N) - \frac{i\Gamma_S|\omega|}{\sqrt{\omega^2 - \Delta^2}} \theta(|\omega| - \Delta) f_S(\omega - \mu_S)$$

Now, multiplying matrices in the expression of $\mathbf{G}^<_{d\sigma}(\omega)$, we get the lesser Green's function for electrons on the QD as

$$\begin{aligned} G^<_{d,11}(\omega) = {} & i\Gamma_N f_N(\omega - \mu_N)|G^r_{d,11}(\omega)|^2 + i\Gamma_N f_N(\omega + \mu_N)|G^r_{d,12}(\omega)|^2 + \\ & \frac{i\Gamma_S|\omega|}{\sqrt{\omega^2 - \Delta_2}} \theta(|\omega| - \Delta) f_S(\omega - \mu_S) \times \\ & \left[|G^r_{d,11}(\omega)|^2 + |G^r_{d,12}(\omega)|^2 - \frac{2\Delta}{|\omega|} Re\Big(G^r_{d,11}(\omega).G^a_{d,12}(\omega)\Big)\right] \end{aligned}$$

where $f_{\alpha \in N,S}(\omega \mp \mu_\alpha) = \left[exp((\omega \mp \mu_\alpha)/k_B T_\alpha) + 1\right]^{-1}$ is the Fermi-Dirac distribution function of reservoirs with temperature T_α and chemical potential $\pm\mu_\alpha$ (measured from Fermi level $\mu_f = 0$).

Acknowledgements Sachin Verma is presently a research scholar at the department of physics IIT Roorkee and is highly thankful to the Ministry of Education (MoE), India, for providing financial support in the form of a Ph.D. fellowship.

References

1. M. Krawiec, Acta Phys. Pol. A **114**, 115 (2008). https://doi.org/10.12693/APhysPolA.114.115
2. K.I. Wysokiński, J. Phys. Condens. Matter. **24**, 335303 (2012). https://doi.org/10.1088/0953-8984/24/33/335303
3. S.Y. Hwang, R. López, D. Sánchez, Phys. Rev. B **91**, 104518 (2015). https://doi.org/10.1103/PhysRevB.91.104518
4. B. Sothmann, R. Sánchez, A.N. Jordan, Nanotechnology **26**, 032001 (2015). https://doi.org/10.1088/0957-4484/26/3/032001
5. S.Y. Hwang, D. Sánchez, R. López, New J. Phys. **18**, 093024 (2016). https://doi.org/10.1088/1367-2630/18/9/093024
6. S.Y. Hwang, R. López, D. Sánchez, Phys. Rev. B **94**, 054506 (2016). https://doi.org/10.1103/PhysRevB.94.054506
7. D. Sánchez, R. López, C. R. Phys. **17**, 1060 (2016). https://doi.org/10.1016/j.crhy.2016.08.005
8. W.P. Xu, Y.Y. Zhang, Q. Wang, Z.J. Li, Y.H. Nie, Phys. Lett. A **380**, 958 (2016). https://doi.org/10.1016/j.physleta.2015.12.032
9. Y. Kleeorin, Y. Meir, F. Giazotto, Y. Dubi, Sci. Rep. **6**, 35116 (2016). https://doi.org/10.1038/srep35116
10. L. Xu, Z. Li, Q. Wang, Y. Nie, AIP Adv. **6**, 125012 (2016). https://doi.org/10.1063/1.4971844
11. G. Benenti, G. Casati, K. Saito, R.S. Whitney, Phys. Rep. **694**, 1–124 (2017). https://doi.org/10.1016/j.physrep.2017.05.008
12. S.-Y. Hwang, D. Sánchez, R. López, Eur. Phys. J. B **90**, 189 (2017). https://doi.org/10.1140/epjb/e2017-80242-1
13. P. Trocha, J. Barnaś, Phys. Rev. B **95**, 165439 (2017). https://doi.org/10.1103/PhysRevB.95.165439
14. S.-Y. Hwang, D. Sánchez, J. Phys. Conf. Ser. **969**, 012139 (2018). https://doi.org/10.1088/1742-6596/969/1/012139
15. H. Yao, C. Zhang, Z.-J. Li, Y.-H. Nie, P.-B. Niu, J. Phys. D Appl. Phys. **51**, 175301 (2018). https://doi.org/10.1088/1361-6463/aab6e4
16. H. Yao, C. Zhang, P.-B. Niu, Z.-J. Li, Y.-H. Nie, Phys. Lett. A **382**, 3220 (2018). https://doi.org/10.1016/j.physleta.2018.08.033
17. M. Kamp, B. Sothmann, Phys. Rev. B **99**, 045428 (2019). https://doi.org/10.1103/PhysRevB.99.045428
18. S. Verma, A. Singh, J. Phys. Condens. Matter. **34**, 155601 (2022). https://doi.org/10.1088/1361-648X/ac4ced
19. S.M. Tabatabaei, D. Sánchez, A.L. Yeyati, R. Sánchez, Phys. Rev. B **106**, 115419 (2022). https://doi.org/10.1103/PhysRevB.106.115419
20. H. Yao, C.-P. Cheng, L.-L. Li, R. Guo, Y. Guo, C. Zhang, Nanoscale Adv. **5**, 1199 (2023). https://doi.org/10.1039/D2NA00838F
21. B. Kumar, S. Verma, Ajay, J. Supercond. Nov. Magn. **36**, 831 (2023). https://doi.org/10.1007/s10948-023-06526-3
22. S.-Y. Hwang, B. Sothmann, D. Sánchez, Phys. Rev. B **107**, 245412 (2023). https://doi.org/10.1103/PhysRevB.107.245412
23. A. Martín-Rodero, A.L. Yeyati, Adv. Phys. **60**, 899–958 (2011). https://doi.org/10.1080/00018732.2011.624266
24. F. Giazotto, T.T. Heikkilä, A. Luukanen, A.M. Savin, J.P. Pekola, Rev. Mod. Phys. **78**, 217 (2009). https://doi.org/10.1103/RevModPhys.78.217
25. E.A. Laird, F. Kuemmeth, G.A. Steele, K. Grove-Rasmussen, J. Nygård, K. Flensberg, L.P. Kouwenhoven, Rev. Mod. Phys. **87**, 703 (2015). https://doi.org/10.1103/RevModPhys.87.703
26. J.P. Pekola, B. Karimi, Rev. Mod. Phys. **93**, 041001 (2021). https://doi.org/10.1103/RevModPhys.93.041001
27. L.D. Hicks, M.S. Dresselhaus, Phys. Rev. B **47**, 12727 (1993). https://doi.org/10.1103/PhysRevB.47.12727
28. L.D. Hicks, M.S. Dresselhaus, Phys. Rev. B **47**, 16631(R) (1993). https://doi.org/10.1103/PhysRevB.47.16631
29. L.D. Hicks, T.C. Harman, X. Sun, M.S. Dresselhaus, Phys. Rev. B **53**, R10493(R) (1996). https://doi.org/10.1103/PhysRevB.53.R10493

30. G.D. Mahan, J.O. Sofo, Proc. Natl. Acad. Sci. U. S. A. **93**, 7436 (1996). https://doi.org/10.1073/pnas.93.15.743
31. M. Josefsson, A. Svilans, A.M. Burke, E.A. Hoffmann, S. Fahlvik, C. Thelander, M. Leijnse, H. Linke, Nat. Nanotech **13**, 920–924 (2018). https://doi.org/10.1038/s41565-018-0200-5
32. M. Josefsson, A. Svilans, H. Linke, M. Leijnse, Phys. Rev. B **99**, 235432 (2019). https://doi.org/10.1103/PhysRevB.99.235432
33. D. Majidi, M. Josefsson, M. Kumar, M. Leijnse, L. Samuelson, H. Courtois, C.B. Winkelmann, V.F. Maisi, Nano Lett. **22**, 630–635 (2022). https://doi.org/10.1021/acs.nanolett.1c03437
34. A.S. Dzurak, C.G. Smith, M. Pepper, D.A. Ritchie, J.E.F. Frost, G.A.C. Jones, D.G. Hasko, Solid State Commun. **87**, 1145–1149 (1993). https://doi.org/10.1016/0038-1098(93)90819-9
35. L. Molenkamp, A.A.M. Staring, B.W. Alphenaar, H. van Houten, C.W.J. Beenakker, Semicond. Sci. Technol. **9**, 903 (1994). https://doi.org/10.1088/0268-1242/9/5S/136
36. D. Prete, P.A. Erdman, V. Demontis, V. Zannier, D. Ercolani, L. Sorba, F. Beltram, F. Rossella, F. Taddei, S. Roddaro, Nano Lett. **91**, 3033–3039 (2019). https://doi.org/10.1021/acs.nanolett.9b00276
37. J. Hubbard, Proc. R. Soc. Lond. A **276**, 238–257 (1963). https://doi.org/10.1098/rspa.1963.0204
38. Hartmut J.W. Haug, A-P. Jauho, Quantum Kinetics in Transport and Optics of Semiconductors:, Solid-State Sciences, **Vol. 123** (Springer-Verlag, Berlin, HD, 2008) Ch.12, p.181. https://doi.org/10.1007/978-3-540-73564-9
39. L.V. Keldysh, Zh. Eksp. Teor. Fiz. **47**, 1515–1527 (1964) [Sov. Phys. JETP **20**, 1018 (1965)]. http://www-thphys.physics.ox.ac.uk/talks/CMTjournalclub/sources/Keldysh.pdf
40. Yigal Meir, Ned S. Wingreen, Phys. Rev. Lett. **68**, 2512 (1992). https://doi.org/10.1103/PhysRevLett.68.2512
41. J.-S. Wang, J. Wang, N. Zeng, Phys. Rev. B **74**, 033408 (2006). https://doi.org/10.1103/PhysRevB.74.033408
42. J.-S. Wang, B.K. Agarwalla, H. Li, J. Thingna, Front. Phys. **9**, 673–697 (2014). https://doi.org/10.1007/s11467-013-0340-x
43. K. Yamamoto, N. Hatano, Phys. Rev. E **92**, 042165 (2015). https://doi.org/10.1103/PhysRevE.92.042165
44. F.C. Wellstood, C. Urbina, J. Clarke, Phys. Rev. B **49**, 5942 (1994). https://doi.org/10.1103/PhysRevB.49.5942
45. J.C. Cuevas, A. Martín-Rodero, A.L. Yeyati, Phys. Rev. B **54**, 7366 (1996). https://doi.org/10.1103/PhysRevB.54.7366
46. T.K. Ng, Phys. Rev. Lett. **76**, 487 (1996). https://doi.org/10.1103/PhysRevLett.76.487